

Statically Balanced Direct Drive Manipulator for Constrained Maneuvers

H. Kazerooni

Mechanical Engineering Department
University of Minnesota
Minneapolis, MN 55455

ABSTRACT

Using a four-bar-linkage, a practical architecture is considered for the University of Minnesota direct drive robot. As a result of the elimination of the gravity forces (without any counter weights), smaller actuators and consequently smaller amplifiers were chosen. The motors yield acceleration of five times the acceleration of gravity at the robot end point without overheating. High torque, low speed, brush-less AC synchronous motors are used to power the robot. Graphite-epoxy composite material is used for the construction of the robot links. A four-node parallel processor has been used to control the robot. The dynamic tracking accuracy, with the feedforward torque method as a control law, has been derived experimentally. The compliance control and its stability condition have been analyzed and demonstrated experimentally.

INTRODUCTION

Direct drive robots have two major advantages over the non-direct drive systems. The first advantage being that; the direct drive arms are free from mechanical backlash and friction due to elimination of transmission systems. A small mechanical backlash in the transmission system would cause the gear teeth to wear faster. The high rate of wear in the gear would develop an even larger backlash. About 25% of the torque in non-direct drive arms is used to overcome the friction [6]. The second advantage is such that the structural stiffness of the direct drive arms are greater than the non-direct drive systems. About 80% of the total mechanical compliance in most non-direct drive industrial robots is caused by transmission systems [7,20]. The high structural stiffness allows for wide bandwidth control. The low structural stiffness of non-direct drive arms, due to the existence of many mechanical elements in the transmission system, is a limiting factor on the achievement of a relatively wide bandwidth control system. One of the significant problems that prohibits the widespread use of existing direct drive robots in industrial applications is their small payload in comparison with the non-direct drive systems. The large payload of the non-direct drive robots is due to the inherent property of the reducer transmission systems. Overheating the motors is another reported disadvantage of the non-direct drive robots. Elimination of the transmission system causes the inertial force and the gravitational force of the links affect the motors directly. In other words, the motors "feel" the inertial and the gravitational forces without any reduction in size. The direct effect of the forces cause the motors to overheat in the direct drive arms. This overheating exists even in the static case when the arm is only under its static load.

The work presented here is on the design and control of the Minnesota direct drive robot [9]. This robot is statically balanced and uses a four-bar-link mechanism (Figure 1) to compensate for some of the drawbacks of the serial [2] and parallelogram types [3] of direct drive robots. Several attempts have been made to improve the manipulator dynamic behavior. Asada and Kanade [2] designed a

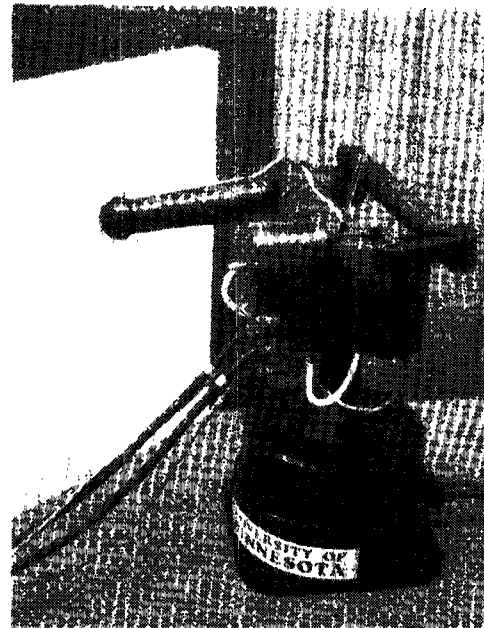


Figure 1: University of Minnesota Direct Drive Robot Arm
serial type direct drive arm in which the actuators were directly coupled to links without any transmission mechanism. The elimination of the transmission mechanism improved the robot performance, however large motors were needed to drive the robot. Asada and Youcef-Toumi [3] studied a direct drive arm with a parallelogram mechanism to eliminate the problems associated with serial type robots. A direct drive arm with a counterweight was designed by Takase et al. [21] in order to eliminate the gravity effect at three major joints. Another direct drive arm, designed by Kuwahara et al. [16] to reduce the effect of gravity using a four-bar-link for the forearm, and a special spring for the upper arm. The counterweight provides the system balance for all possible positions, however it increases the total inertia of the robot arm. The spring balancing will not perfectly balance the system either [18]. In this research, a statically balanced direct drive arm is designed to achieve improved dynamic behavior.

ARCHITECTURE

The architecture of this arm is such that the gravity term is completely eliminated from the dynamic equations. This balanced mechanism is designed without adding any extra counterbalance weights. The new features of this new design are as follows:

1. Since the motors are never affected by gravity, the static load will

be zero. Hence no overheating results in the system in the static case.

2. The elimination of gravity terms calls for smaller motors with less stall torque (and consequently smaller amplifiers) which have been chosen for a desired acceleration.

3. With the lack of gravity terms, higher accuracy can be achieved. This is true because the links have steady deflection due to constant gravity effect. This gives better accuracy and repeatability for fine manipulation tasks.

4. As depicted in Figure 3, the architecture of this robot allows for a "large" workspace. The horizontal workspace (radius = 80 cm) of this robot is quite attractive from the stand point of manufacturing tasks such as assembly and deburring.

5. Graphite-epoxy composite material is used for the construction of the robot links. This robot is light (60 kg) and can be mounted on an autonomous vehicle. The pay load without losing precision is 2 kg.

The arm has three degrees of freedom, all of which are articulated drive joints (Figure 10 shows the schematic of the robot where the links are numbered). Motor 1 powers the system about a vertical axis. Motor 2 pitches the entire four-bar-linkage while motor 3 is used to power the four-bar-linkage. Link 2 is directly connected to the shaft of motor 2. Figure 3 shows the top view and side view of the robot. The coordinate frame $X_1Y_1Z_1$ has been assigned to link 1 of the robot for $i=1,2,\dots,5$. The center of coordinate frame $X_iY_iZ_i$ corresponding to link 1 is located at point O as shown in figure 2. The center of the inertial global coordinate frame $X_0Y_0Z_0$ is also located at point O (The global coordinate frame is not shown in the figures). The joint angles are represented by θ_1 , θ_2 , and θ_3 where θ_1 represents the rotation of link 1 (coordinate frame $X_1Y_1Z_1$ coincides on the global coordinate frame $X_0Y_0Z_0$ when $\theta_1=0$), θ_2 represents the pitch angle of the four-bar-linkage as shown in Figure 2, and θ_3 represents the angle between link 2 and link 3. Shown are the conditions under which the gravity terms are eliminated from the dynamic equations.

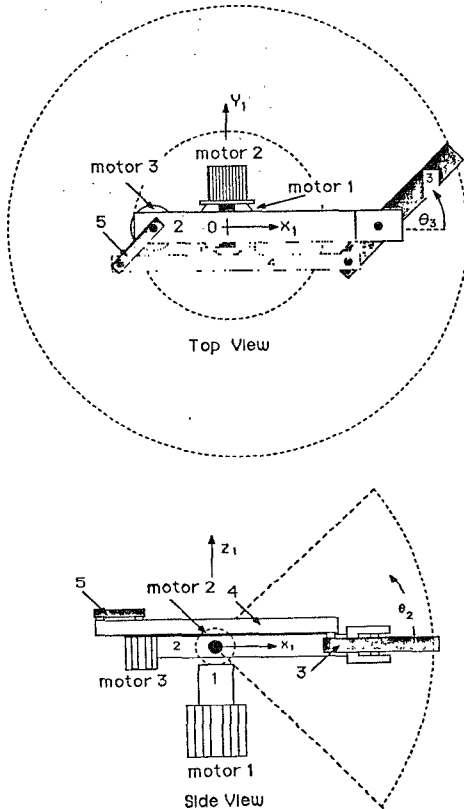


Figure 2: The Side View and Top View of the Robot

Figure 3 shows the four-bar-linkage with assigned coordinate frames. By inspection the conditions under which the vector of gravity passes through origin, O, for all possible values of θ_1 and θ_3 are given by equations (1) and (2) where m_i, L_i are mass and length of each link, \bar{x}_i is the distance of center of mass from the origin of each coordinate frame, and m_{t3} is mass of motor 3.

$$(m_3\bar{x}_3 - m_4L_5 - m_5\bar{x}_5) \sin \theta_3 = 0 \quad (1)$$

$$g(m_{t3} + m_5) - m_2\bar{x}_2 - m_3(L_2 - g) - m_4(\bar{x}_4 - g) - [m_3\bar{x}_3 - m_4L_5 - m_5\bar{x}_5] \cos \theta_3 = 0 \quad (2)$$

Conditions (1) and (2) result in the following equations:

$$m_3\bar{x}_3 - m_4L_5 - m_5\bar{x}_5 = 0 \quad (3)$$

$$g(m_{t3} + m_5) - m_2\bar{x}_2 - m_3(L_2 - g) - m_4(\bar{x}_4 - g) = 0 \quad (4)$$

If equations (3) and (4) are satisfied, then the center of gravity of the four-bar-linkage passes through point O for all the possible configurations of the arm. Note that the gravity force still passes through O even if the plane of the four-bar-linkage is tilted by motor 2 for all values of θ_2 .

Since at low speeds, AC torque motors do not tend to cog; low speed, high torque, and brush-less AC synchronous motors have been chosen to power the robot. Each motor consists of a ring shaped stator and a ring shaped permanent magnet rotor with a large number of poles. The rotor is made of rare earth magnetic material (Neodymium) bonded to a low carbon steel yoke with structural adhesive. The stator of the motor (with winding) is fixed to the housing for heat dissipation. To develop wide bandwidth (high speed) closed loop control for the robot, Graphite-epoxy composite and AA7075T6 Materials were used to construct the links. The high structural stiffness and low density of the Graphite-epoxy composite result in high natural frequencies in the robot dynamics. The higher the natural frequencies are, the wider the bandwidth and consequently faster the closed loop system will be [14]. A strong bond between the composite parts and the aluminum parts was achieved using an epoxy adhesive (3M Epoxy Adhesive EC - 3569 B/A). To minimize joint clearance and reduce bearing mass, Super Precision angular contact bearings (ABEC- 7, extremely light series 1900) were used.

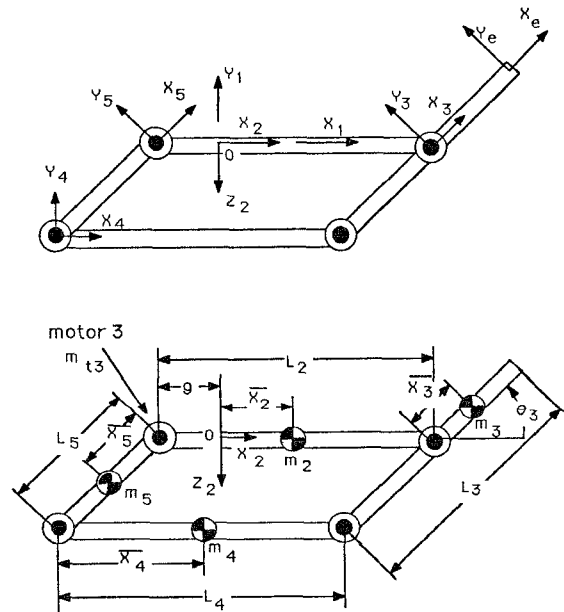


Figure 3: Four Bar Link Mechanism

FORWARD KINEMATICS

The forward kinematic problem is to compute the position of the end point in the global coordinate frame $X_0Y_0Z_0$, given the joint angles, θ_1 , θ_2 , and θ_3 . The end point position of the robot relative to the global coordinate frame is characterized by P_x , P_y , and P_z in the global coordinate frame $X_0Y_0Z_0$:

$$P_x = (C_1C_2C_3 - S_1S_3) (L_3 - L_5) + C_1C_2(L_2 - g) \quad (5)$$

$$P_y = (S_1C_2C_3 + C_1S_3)(L_3 - L_5) + S_1C_2(L_2 - g) \quad (6)$$

$$P_z = S_2(L_2 - g) + S_2C_3(L_3 - L_5) \quad (7)$$

where $S_i = \sin(\theta_i)$, and $C_i = \cos(\theta_i)$.

INVERSE KINEMATICS

The closed-form of inverse kinematics of the proposed arm derived using the standard method [6,19]. The joint angles for the given end point position can be determined using the following equations:

$$\theta_1 = \text{atan2}(P_y, P_x) - \text{atan2}((L_3 - L_5) \sin \theta_3) \pm [P_x^2 + P_y^2 - (L_3 - L_5)^2 \sin^2 \theta_3]^{1/2} \quad (8)$$

$$\theta_2 = \sin^{-1} \left\{ P_z / [(L_2 - g) + (L_3 - L_5) \cos \theta_3] \right\} \quad (9)$$

$$\theta_3 = \cos^{-1} \left\{ [P_x^2 + P_y^2 + P_z^2 - (L_2 - g)^2 - (L_3 - L_5)^2] / [2(L_2 - g)(L_3 - L_5)] \right\} \quad (10)$$

HARDWARE

A schematic of the system hardware is shown in Figure 4. An IBM/AT microcomputer which is hosting a four-node NCUBE parallel processor is used as the main controller of this robot. The parallel processor has four nodes and a PC/AT bus interface. Each node is an independent 32-bit processor with local memory and communication links to the other nodes in the system. A high speed AD/DA converter has been used for reading the velocity signals and sending analog command signals to the servo controller unit. A parallel IO board (D/D converter) between the servo controller unit and the computer allows for reading the R/D (Resolver to Digital) converter.

The servo controller unit produces three phase, Pulse Width Modulated (PWM), sinusoidal currents for the power amplifier. The servo controller unit contains an interpolator, R/D converter and a communication interface for the computer. The servo controller unit can be operated in either a closed loop velocity or current (torque) control mode (the current control is used). A PWM power amplifier, which provides up to 47 Amperes of drive current from a 325 volt power supply, is used to power the motors. The main DC bus power is derived by full-wave rectifying the three phase 230VAC incoming power. This yields a DC bus voltage of 325VDC.

The actuators used in this robot are neodymium (NdFeB) magnet AC brushless synchronous motors. Due to the high magnetic field strength (maximum energy products: 35 MGOe) of

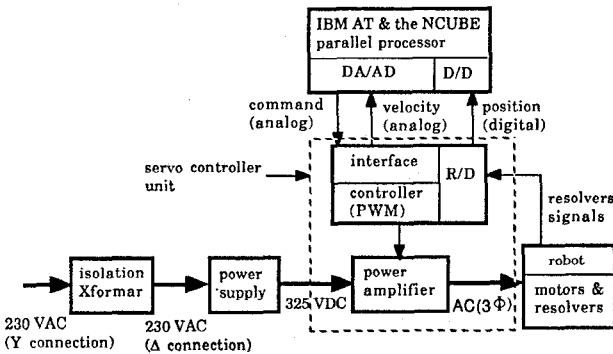


Figure 4: The Control Hardware for Minnesota Robot

the rare earth NdFeB magnets, the motors have high torque to weight ratio. Pancake type resolvers are used as position and velocity sensors. The peak torque of motor 1 is 118 Nm, while the peak torques of motors 2 and 3 are 78 and 58 Nm respectively.

EXPERIMENTAL RESULTS

We describe two sets of experiments in this article. First, the performance of the robot is measured in unconstrained space as a tracking accuracy along a specified trajectory. Second, the stability of the robot in constrained maneuvers has been analyzed and verified experimentally. In constrained maneuvers, the contact forces must be accommodated rather than resisted [8, 10-13].

A feedforward compensator, as shown in Figure 5 is used to cancel the robot nonlinear terms while a set of constant gains are used in the feedback loop to decrease the error and develop robustness in modeling errors. Because this robot does not contain any gearing, frictional losses are small and consequently the manipulator, using Lagrangian approach [5,17] can be modeled by equation 11.

$$M(\theta) \ddot{\theta} + C(\theta, \dot{\theta}) = \tau - J^T f \quad (11)$$

where $\ddot{\theta}$, $\dot{\theta}$, θ are vectors containing the joints' accelerations, velocities, and positions, respectively; $M(\theta)$ is the inertia matrix; $C(\theta, \dot{\theta})$ is the vector representing the coriolis and centrifugal forces, τ is the vector of joint torques, J^T is the jacobian transpose matrix, and f is the vector of external forces applied at the robot endpoint. The $M(\theta)$ and $C(\theta, \dot{\theta})$ functions for the University of Minnesota Robot have been computed in closed form and the coefficients for these functions have been experimentally identified [9].

Trajectory control for the manipulator is performed by a digital implementation of a feedforward torque controller, which is given by:

$$\tau = K_p(\theta_d - \theta) + K_v(\dot{\theta}_d - \dot{\theta}) + \hat{M}(\theta_d) \ddot{\theta}_d + \hat{C}(\theta_d, \dot{\theta}_d) \quad (12)$$

where τ is the vector of joint torques; $(\theta_d - \theta)$ is the error between the command position, θ_d , and the actual position, θ , and $(\dot{\theta}_d - \dot{\theta})$ is the error between the respective velocities. K_p is a 3x3 diagonal matrix containing the position gains. K_v is a 3x3 diagonal matrix containing the velocity gains. $\hat{M}(\theta_d)$ is the estimated, inertia matrix; and $\hat{C}(\theta_d, \dot{\theta}_d)$ is the estimated, 3x1 vector of centrifugal and coriolis forces. The physical reasoning behind this control law is that the nonlinear feedforward terms, $\hat{M}(\theta_d)$ and $\hat{C}(\theta_d, \dot{\theta}_d)$, tend to cancel the effects of nonlinear effects of $M(\theta)$ and $C(\theta, \dot{\theta})$ in the robot's dynamics and result in a nearly uncoupled, linear system. The $\text{Kin}(\cdot)$ operator in the diagram represents the forward kinematics, while $\text{Kin}^{-1}(\cdot)$ represents the inverse kinematics. When the trajectory is specified in cartesian space as a function of time, $e(t)$, the inverse kinematics and numerical differentiation are employed to transform it into joint space, $\theta_d(t)$.

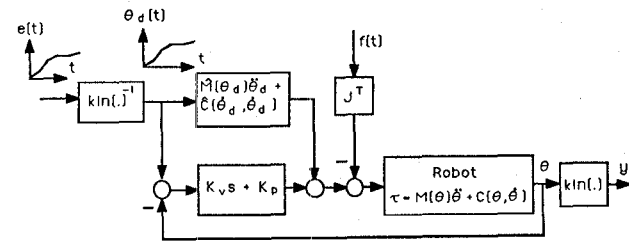


Figure 5: Robot and Feedforward Torque Controller Dynamics (1,4)

The reference trajectory in the experiment is generated by a cubic polynomial. All the joints were commanded to simultaneously move 30 degrees in 0.3 seconds from a predetermined origin (Figure 6). The maximum velocity and acceleration for each joint are 150 degree/sec and 2000 degree/sec², respectively. The robot control program, written in C language, yields a 250 Hz sampling frequency. The trajectory error plots for each joint are depicted in Figure 7 where the peak trajectory errors are 0.7°, 1.2° and 0.44° for joints 1, 2 and 3 respectively.

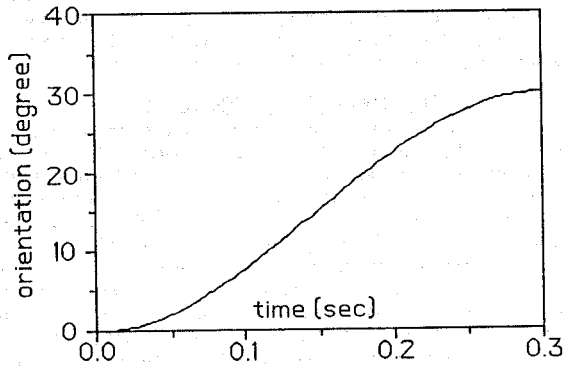


Figure 6: Commanded Trajectory for Each Motor

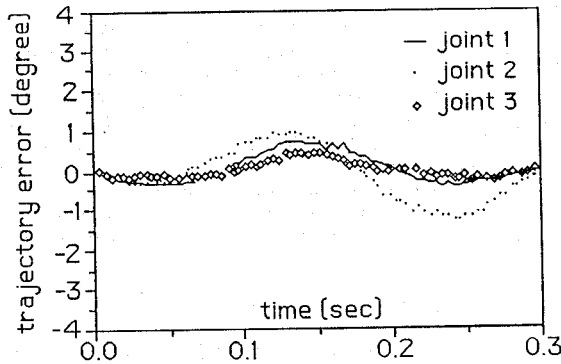


Figure 7: Trajectory Error; all the parameters are experimentally identified [9].

Although feedforward torque control is computationally efficient, this method does not achieve perfect uncoupling of each joint. Using equations 11 and 12 and assuming that $\mathcal{C}(\theta_d, \dot{\theta}_d) \approx \mathcal{C}(\theta, \dot{\theta})$ and $\dot{M}(\theta_d) \approx \dot{M}(\theta)$, a differential equation in terms of the joint accelerations is obtained:

$$\ddot{\theta} - \ddot{\theta}_d + M(\theta)^{-1} [K_p (\theta_d - \theta) + K_v (\dot{\theta}_d - \dot{\theta})] - M(\theta)^{-1} J^T f \quad (13)$$

Note that despite the assumption that the robot dynamics are accurately known, the joints are not perfectly uncoupled, and the degree of coupling varies as a function of the configuration.

The second set of experiments concerns the performance of the robot in constrained maneuvers. Figure 8 shows the system

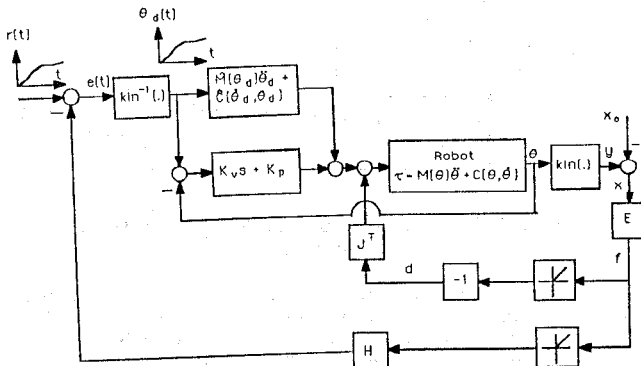


Figure 8: Trajectory Controller, Robot Dynamics, Environment Dynamics, and Compliance Compensator.

architecture when the robot interacts with the environment and when the robot compliancy is tailored by means of an H compensator. The H block is a part of the compliance controller and is implemented in the digital controller. The product of the environment mapping, E, is an external force, f, which is expressed in the global cartesian coordinate frame. Although the trajectory controller operates in the manipulator joint space, H has been implemented as linear transfer function which can accept the cartesian force and produce a cartesian displacement. The product of H is a small displacement. In practice, $r(t)$ is transformed into joint space prior to execution; the inverse Jacobian, J^{-1} , is substituted for $\text{kin}^{-1}(\cdot)$ in the system. The command, $r(t)$ is used for both constrained and unconstrained maneuvers. When the robot is not in contact with the environment, $f=0$ and the robot is driven by its tracking controller, $r(t)$. When the robot comes in contact with the environment, then contact force follows the input command, $r(t)$.

To guarantee the stability of the system of Figure 8, H must be chosen such that inequality 14 is satisfied [15].

$$\gamma < \frac{1}{\alpha} \quad (14)$$

where α is the supremum of $\sigma_{\max}(J^{-T} K_p J^{-1})$ over the commanded trajectory and $\gamma = \sigma_{\max}(N)$. σ_{\max} indicates the maximum singular value¹, and N is a matrix whose ijth entry is $\sup_{\omega} |H_{ij}|$. In other words, each member of N is maximum value of $|H_{ij}|$ over all $\omega \in [0, \infty)$. Equivalently one can satisfy inequality 15.

$$\gamma < \text{infimum of } \sigma_{\min}(J K_p^{-1} J^T) \text{ over the trajectory}^2 \quad (15)$$

One must calculate the minimum singular value of $(J K_p^{-1} J^T)$ at each point in the commanded trajectory. The infimum is the lowest of all the minimum singular values. The gain of H (expressed in terms γ) must be chosen smaller than this infimum. From inequality 15, the stability region will approach zero when the robot maneuvers near a singular point ($\det(J) \rightarrow 0$) and/or when the position gains approach infinity. Both cases are instances of "infinite stiffness" for the robot, the first is due to the robot configuration, while the second is due to the tracking controller.

For a sufficient stability condition, if the condition is satisfied, the stability is guaranteed; however, if the condition is violated, no conclusion can be made. In the first experiment, we design an H such that inequality 15 is satisfied and show, through experiment, that the system is stable. In the second experiment, we show that an H which destabilizes the system also violates inequality 15.

A reinforced aluminum wall was mounted vertically in the robot workspace as shown in Figure 9 to simulate a stiff environment. Motor 2 was mechanically locked while motors 1 and 3 were used to actuate the robot for horizontal maneuvering; this resulted in planar, horizontal motion of the robot endpoint in global, cartesian space. A force sensor is mounted on the manipulator endpoint to measure contact forces. Figure 10 shows the top view of experimental set up.

Since the experiments are all two-dimensional, H is a 2×2 matrix operating on contact forces which are normal and tangential to the wall. (The endpoint force measurements were resolved into the global coordinate frame.) In these experiments, only the compliancy in the direction normal to the wall was

¹ The maximum singular value of a matrix A, $\sigma_{\max}(A)$ is defined as:

$$\sigma_{\max}(A) = \max \frac{|Az|}{|z|}$$

where z is a non-zero vector and $|\cdot|$ denotes the Euclidean norm.

² To guarantee the stability of the system, H must be chosen such that its "size" is smaller than the "size" of the sensitivity of the robot. We define the robot sensitivity in a global coordinate frame as a mapping from the imposed forces on the robot to the robot position. The response of mechanical systems for a given driving force is larger if the systems are lighter and less damped. Therefore, the largest value for the sensitivity function arises when $M(\theta)=0$ and $K_v(\dot{\theta}_d - \dot{\theta})=0$. This largest sensitivity is $J^{-T} K_p J^{-1}$. For a slower derivation of this stability condition, see reference 15.

supplemented, so the following form of H was chosen:

$$H = \begin{bmatrix} \frac{H_0}{Ts+1} & 0 \\ 0 & 0 \end{bmatrix} \quad (16)$$

where T is empirically chosen constant and is used to filter the high frequency noise in the force measurement. T was fixed at 0.05 for all the experiments. The function, $r(t)$, shown in Figure 10 by the dashed line, is chosen as the assigned trajectory to the robot. Since H has only one non-zero member, then γ will be the maximum value of the magnitude of $H_0/(Tj\omega + 1)$. The maximum value of H is H_0 and occurs at DC ($\omega=0$).

In the first experiment, we show that if inequality 15 is satisfied for a maneuver shown in Figure 10, then the robot can interact with the environment stably. Figure 11 shows the maximum and minimum singular values of $(J K_p^{-1} J^T)$ evaluated for all configurations along the trajectory. We choose H_0 to be .0003 so $H(s)$ was smaller than $\sigma_{\min}(J K_p^{-1} J^T)$ for all configurations within the maneuver. Figure 12 shows the experimental and simulated values of the normal contact force. The stable contact was indicated by the absence of undamped oscillations in the normal force.

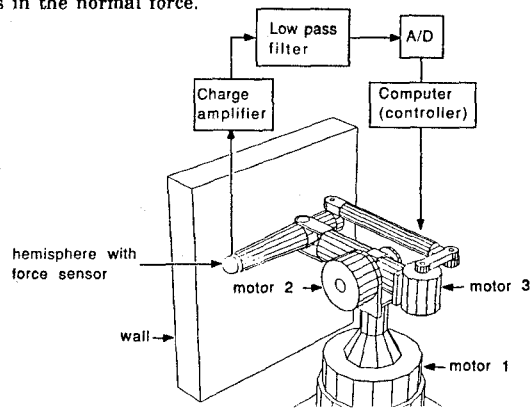


Figure 9: University of Minnesota Robot in Constrained Maneuvers

In the second experiment, H_0 was set to .0015. Figure 13 shows the experimental and simulated values of the normal contact force as a function of time. In both results, the contact force oscillate throughout the maneuver, indicating that the compliance controller was unstable. The comparison with the singular value plot in Figure 11, shows that H_0 exceeded the lower bound on $\sigma_{\min}(J K_p^{-1} J^T)$; hence, the stability condition has been violated. Since inequality 15 is only a sufficient condition for stability, violation of this condition does not lead to any conclusion. Figure 14 shows the experimental and simulated contact force when $H_0=0.0005$. The system was stable yet the stability condition has not been satisfied.

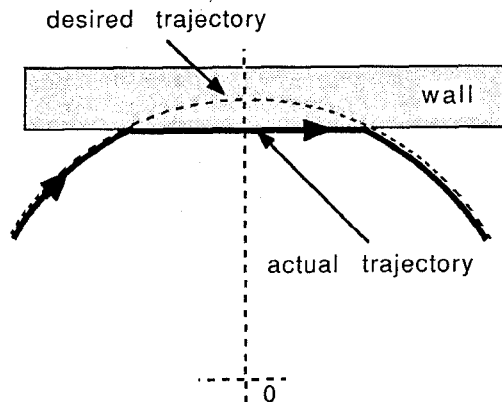


Figure 10: The top view of the experimental setup. The dashed line is the desired end point trajectory while the solid line is the actual trajectory.

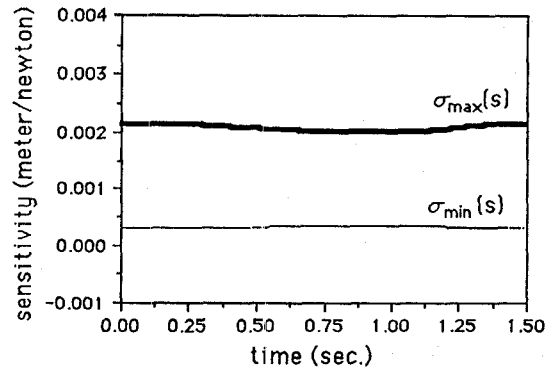


Figure 11: The maximum and minimum singular values of the sensitivity function for the actual trajectory shown in Figure 10.

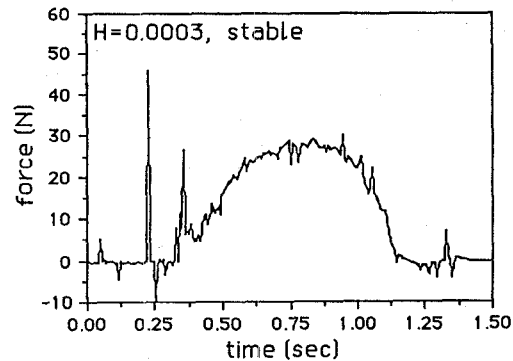


Figure 12: Experimental measurement and simulated value of the stable normal contact force. $H_0 = 0.0003$ satisfies the stability condition.

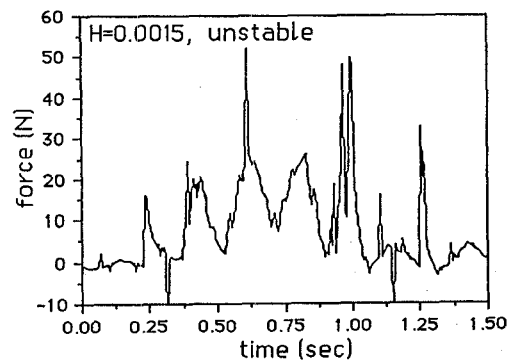


Figure 13: Experimental measurement and simulated value of the unstable normal contact force. $H_0 = 0.0015$ does not satisfy the stability condition.

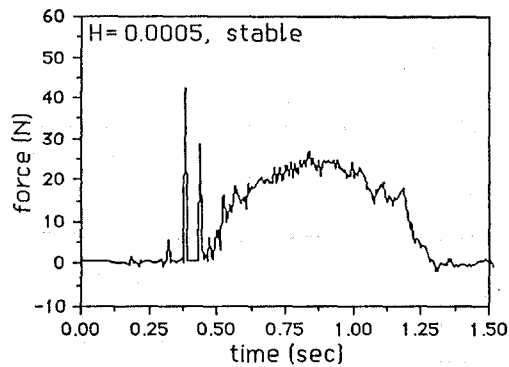


Figure 14: Experimental measurement and simulated value of the normal contact force.
 $H_0 = 0.0005$ violates the stability condition, however the system is stable.

SUMMARY

This paper presents some results of the on-going research project on a statically-balanced direct drive arm at the University of Minnesota. The statically-balanced mechanism without counter weights allows for selection of smaller actuators. Since in static or quasi-static operations, there is no load on the actuators, the overheating of the previous direct drive robots is alleviated. The robot links are made of graphite-epoxy composite materials to give more structural stiffness and less mass. The high structural stiffness and low mass of the links allow for the wide bandwidth of the control system. To improve tracking errors, the robot parameters were identified experimentally. The errors in the trajectory and velocity were reduced significantly. Stability of the robot when it interacts with a hard environment has been derived and experimentally verified.

REFERENCES

1. An, C. H., Atkeson, C. G., Hollerbach, J. M., "Experimental Determination of the Effect of Feedforward Control on Trajectory Tracking Errors", IEEE International Conference on Robotics and Automation, San Francisco, CA, Vol. 1, pp. 55-60, April 1986.
2. Asada, H., Kanade, T., "Design of Direct Drive Mechanical arms", ASME Journal of Vibration, Acoustics, Stress, and Reliability in Design, Vol. 105, No. 3, pp. 312-316, July 1983.
3. Asada, H., Youcef-Toumi, H., "Analysis and Design of a Direct Drive Arm with a Five-Bar-Link Parallel Drive Mechanism", ASME Journal of Dynamic Systems, Measurement and Control, Vol. 106, No. 3, pp. 225-230, 1984.
4. Asada, H., Kanade, T., Takeyama, I., "Control of a Direct Drive Arm", Journal of Dynamic Systems, Measurements, and Control, Vol. 105, pp. 136-142, September 1983.
5. Asada, H., Slotine, J.-J.E., "Robot Analysis and Control", John Wiley and Sons: New York, NY, 1986.
6. Craig, J. J., "Introduction to Robotics: Mechanics and Control", Addison-Wesley: Reading, Massachusetts, 1986.
7. Forrest-Barlach, M. G., Babcock, S. M., "Inverse Dynamics Position Control of a Compliant Manipulator", IEEE 1986 International Conference on Robotics and Automation, Vol. 1, pp. 196-205, April 1986.
8. Hogan, N., "Impedance Control, An Approach Manipulation", ASME Journal of Dynamic Systems, Measurement, and Control, Vol. 107, No.1, pp.1-24, March, 1985.
9. Kazerooni, H., Kim, S., "A New Architecture for Direct Drive Robots", In proceeding of the IEEE International Conference on Robotics and Automation, Philadelphia, PA, Vol. 2, pp. 1166-1172, April 1988.
10. Kazerooni, H., Sheridan, T. B., Houpt, P. K., "Fundamentals of Robust Compliant Motion for Robot Manipulators", IEEE Journal on Robotics and Automation, Vol. 2, No. 2, pp. 83-92, June 1986.
11. Kazerooni, H., Houpt, P. K., Sheridan, T. B., "Design

- Method for Robust Compliant Motion for Robot Manipulators", IEEE Journal on Robotics and Automation, Vol. 2, No. 2, pp. 93-105, June 1986.
12. Kazerooni, H., Tsay, T. I., "Stability Criteria for Robot Compliant Maneuvers", In proceeding of the IEEE International Conference on Robotics and Automation, Philadelphia, PA, Vol. 2, pp. 1166-1172, April 1988.
13. Kazerooni, H., "Direct-Drive Active Compliant End Effector (Active RCC)", IEEE Journal on Robotics and Automation, Vol. 4, No. 3, pp. 324-333, June 1988.
14. Kazerooni, H., Houpt, P. K., "On the Loop Transfer Recovery", International Journal of Control, Vol. 43, No. 3, pp. 981-996, 1986.
15. Kazerooni, H., Kim, S., Waibel, B. J., "Theory and Experiments on the Robot Compliance Control", ASME Winter Annual Meeting, "Robotics", Chicago, Dec. 1988.
16. Kuwahara, H., One, Y., Nikaido, M., Matsumoto, T., "A Precision Direct Drive Robot Arm", In Proceedings of American Control Conference, Vol. 2, pp. 722-727, Boston, MA, 1985.
17. Luh, J. Y. S., Walker, M. W., Paul, R. P., "Resolved - Acceleration Control of Mechanical Manipulators", IEEE Transactions on Automatic Control, Vol. AC25, No. 3, pp. 468-474, June, 1980.
18. Mahalingam, S., and Sharan, A. M., "The Optimal Balancing of the Robotic Manipulators", IEEE 1986 International Conference on Robotics and Automation, San Francisco, CA, Vol. 2, pp. 828-835, April 1986.
19. Paul, R. P., "Robot Manipulators: Mathematics, Programming, and Control", MIT press, Cambridge, MA, 1981.
20. Rivin, E. I., "Effective Rigidity of Robot Structures: Analysis and Enhancement", Proceedings of 85 American Control Conference, Vol. 1, pp. 381-382, Boston, MA, 1985.
21. Takase, K., Hasegawa, T., Suehiro, T., "Design and Control of a Direct Drive Manipulator", Proceedings of the International Symposium on Design and Synthesis, Tokyo, Japan, pp. 333-338, July 1984.